Ceramic vacuum chamber with a strip-patterned metallic coating to suppress eddy currents for beam injection in next-generation light sources

M. Tajima,[1,*] K. Fukami,[1,2] M. Masaki,[1] T. Ohshima,[1,2] M. Shoji,[1,2] S. Takano,[1,2] K. Tamura,[1,2] T. Taniuchi,[1] and H. Tanaka[2]

[1]*Japan Synchrotron Radiation Research Institute (JASRI), 1-1-1 Kouto, Sayo, Hyogo 679-5198, Japan*
[2]*RIKEN SPring-8 Center (RSC), 1-1-1 Kouto, Sayo, Hyogo 679-5148, Japan*

(Received 11 January 2026; accepted 29 May 2026; published 9 July 2026)

Transparent top-up injection is important for maintaining photon beam stability and brightness in next-generation light sources. In traditional off-axis injection based on pulsed orbit bumps employing dipole kicker magnets, the injection transparency relies on the precise matching of magnetic fields to ensure a closed local orbit bump throughout the pulse duration. Similarly, alternative off-axis injection based on nonlinear kickers necessitates rigorous control of the magnetic field near the stored beam orbit. A key challenge common to both is mitigating the distortion of the pulsed kicker magnetic field caused by eddy currents in the metallic coating of the ceramic vacuum chamber, while simultaneously minimizing beam coupling impedance and heat load. This paper addresses this issue through the design of a ceramic vacuum chamber aimed at next-generation light sources, tailored to the requirements of the SPring-8 upgrade, SPring-8-II. We prototyped a ceramic vacuum chamber equipped with a strip-patterned titanium coating on its inner surface. Experimental characterization demonstrated that field deviations caused by eddy currents in the coating can be reduced to approximately 0.1% of the peak value throughout a pulse duration as short as 4 μs. These results satisfy the design requirements for beam injection in SPring-8-II.

DOI: 10.1103/vml2-pycy

I. INTRODUCTION

Photon beam stability is a critical requirement for synchrotron radiation facilities. In next-generation light sources with emittances reduced by orders of magnitude [1–4], the horizontal beam size shrinks to several tens of micrometers, leading to a significantly reduced beam lifetime. Top-up injection is therefore essential to compensate for the rapid decay of the stored electron beam current. An established method is off-axis beam injection, which typically uses multiple kicker magnets to create a horizontal local orbit bump at the time of injection. However, imperfect closure of the orbit bump during injection causes transient oscillations of the stored beam, thereby degrading the effective brightness. In next-generation facilities, the oscillation amplitude must be kept below the beam size, down to several micrometers, to suppress the brightness reduction and ensure transparent injection for photon users. Such transparency relies on the precise matching of magnetic fields between the kicker magnets. To obviate this requirement, alternative off-axis injection schemes have been developed using nonlinear kickers [5–8] that aim for rigorous control of the magnetic field near the stored beam orbit. Ceramic vacuum chambers are widely used in conjunction with these kickers to avoid the shielding effects of eddy currents inherent in metal chambers. Nevertheless, a key challenge common to both traditional dipole kickers and nonlinear kickers remains: mitigating the distortion of the kicker magnetic field caused by eddy currents within the metallic coating of the ceramic vacuum chamber, while simultaneously minimizing beam coupling impedance and heat load.

The ongoing SPring-8-II upgrade plan in Japan [3] aims to achieve transparent beam injection while utilizing a local orbit bump for off-axis injection [9]. Our proposed scheme is strategically designed to leverage the capabilities of high-brightness, low-emittance injector provided by SACLA [10]. Based on the current SPring-8 off-axis injection system, which enables a stable and reliable top-up operation [11], our scheme minimizes the injection amplitude to fit within the dynamic aperture and ensures transparent top-up capability. The proposed beam injection scheme is illustrated in Fig. 1. Two identical kicker magnets with the same kick angle, referred to as twin kickers, will be placed on the beam injection section of the storage ring to provide an orbit bump for off-axis beam injection. A linear π-bump scheme is adopted, where the horizontal betatron phase advance between the kickers is

*Contact author: minori.tajima@spring8.or.jp

Published by the American Physical Society under the terms of the Creative Commons Attribution 4.0 International license. Further distribution of this work must maintain attribution to the author(s) and the published article's title, journal citation, and DOI.

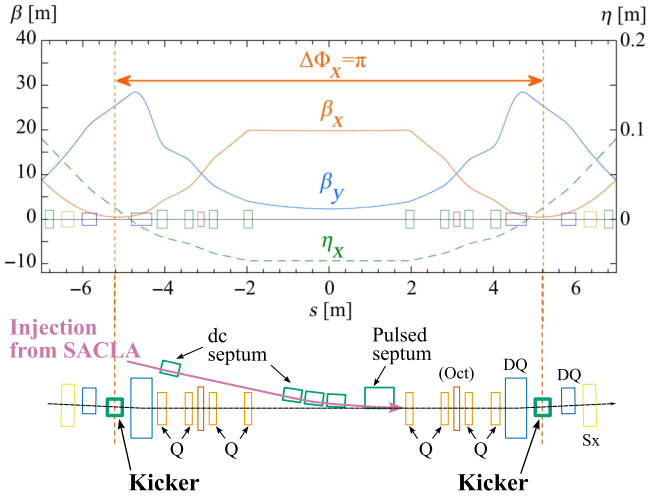

FIG. 1. Optics design (top) and schematic setup (bottom) for the proposed beam injection scheme for SPring-8-II. Q, DQ, Sx, Oct represent quadrupole, DQ combined-function, sextupole, octupole magnets, respectively, while octupoles are used for commissioning only.

set to π, nonlinear magnets such as sextupoles are excluded from the orbit bump, and the quadrupoles are designed to provide sufficiently wide good-field regions to suppress nonlinear field components at the bumped beam positions. A new kicker magnet [12] and a pulsed power supply [13] have already been developed to achieve pulsed magnetic field matching within 0.1% of the peak value over the entire duration of the orbit bump. The remaining critical component is the ceramic vacuum chamber, installed within the kicker magnets' pole gap. Our goal is to achieve the same level of magnetic field matching (0.1%) even in the presence of the ceramic chamber.

The inner surface of the ceramic chambers is coated with a thin metallic layer to provide a conductive path for the image currents of the stored beam, thereby reducing beam coupling impedance and heat load. Titanium (Ti) is widely used due to its nonmagnetic properties and relatively low electrical conductivity, which allows for a manageable coating thickness that suppresses eddy currents and relaxes tight manufacturing tolerances. Several developments have been reported aiming to prevent magnetic field distortion due to the eddy currents while simultaneously minimizing parasitic heating; these are, in principle, conflicting requirements. While patterned coatings have been investigated previously [14–17], suppression of the magnetic field deviations to within 0.1% of the peak over the entire duration of the pulse has not yet been demonstrated.

This paper presents the design and experimental verification of a ceramic vacuum chamber featuring a patterned titanium coating on its inner surface, aimed at realizing transparent beam injection in next-generation light sources, with its feasibility evaluated against the specifications of SPring-8-II for future implementation.

II. DESIGN

The design of the Ti coating on the ceramic chamber must balance two conflicting requirements: minimizing beam coupling impedance and ensuring transparency to the kicker's pulsed magnetic field. First, we optimized the coating thickness to manage beam coupling impedance and related heating power. To determine the minimum required coating thickness, the dependence of longitudinal impedance on the coating thickness was evaluated using the analytical formula [18] available for the case of a ceramic cylinder (length L, radius b, wall thickness d_c) with a uniform Ti coating (thickness d, resistivity $\rho = 0.55$ μΩm) on its inner surface:

$$\frac{Z_\parallel}{L} = \frac{-i}{2\pi\epsilon_0 cb}\left\{\left(\frac{a}{k}-\frac{k}{a}\right)\frac{1+A\tanh(ad)}{A+\tanh(ad)}-\frac{kb}{2}\right\}^{-1}, \quad (1)$$

where $k = \omega/c$, $a = [1 - i\,\mathrm{sgn}(\omega)]/d_s$, $\nu = (\mu_r\epsilon_r - 1)^{1/2}$, $A = \nu(a/k - k/a)\tan(\nu d_c)/k\epsilon_r$, $d_s = \sqrt{2\rho/(\omega\mu_0)}$ is skin depth, μ_r and ϵ_r are relative permeability and permittivity of the ceramic, respectively. From this impedance, the loss factor, which determines the heating power, was evaluated for various Ti coating thicknesses by

$$\frac{1}{\pi}\int_0^\infty \mathrm{Re}(Z_\parallel(\omega)e^{-\omega^2\sigma_t^2})\mathrm{d}\omega \quad (2)$$

as a function of bunch length σ_t (in rms). Figure 2 shows an example of the result using representative parameters for a kicker magnet ceramic vacuum chamber: $b = 18$ mm, $d_c = 3$ mm, $L = 400$ mm, $\mu_r = 1$, and $\epsilon_r = 9.9$. To mitigate the heating power, a minimum coating thickness of 6 μm is required for our design as the heating power was observed to plateau for coating thicknesses exceeding 6 μm.

Next, a strip-patterned coating was implemented instead of a uniform one to mitigate eddy currents in the Ti coating. The strip width was then optimized to minimize

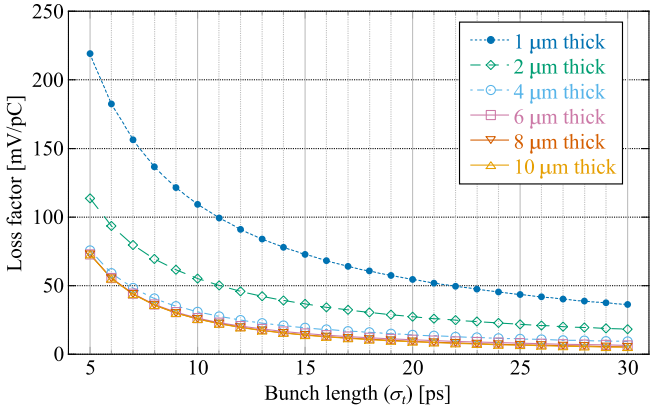

FIG. 2. Loss factor of a uniformly coated cylinder calculated at various coating thicknesses.

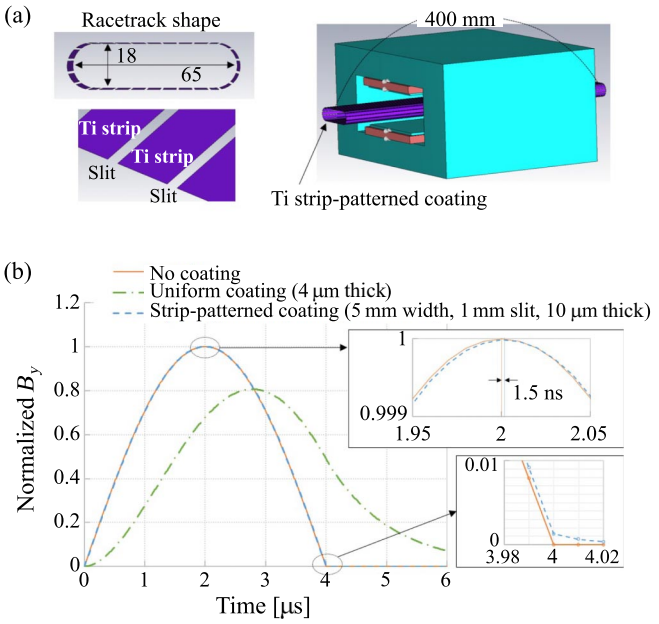

FIG. 3. (a) 3D simulation model integrated with a kicker magnet, used for evaluating the magnetic field deviation caused by eddy currents induced in the Ti strip-patterned coating. (b) Calculated magnetic field strength at the center of the magnetic pole gap for a no-coating case (orange solid line), a 4 μm thick uniform coating (green dash-dotted line), and a 10 μm thick strip-patterned coating with 5 mm width and 1 mm slits (blue dashed line).

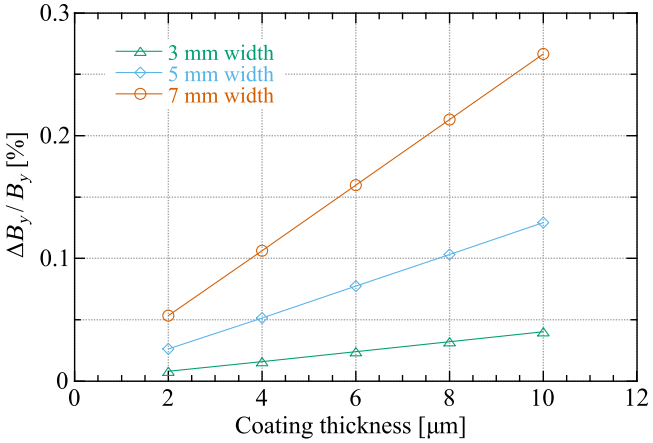

FIG. 4. Simulated magnetic field deviation relative to the no-coating case as a function of Ti coating thickness. Results are shown for strip widths of 3, 5, and 7 mm, with a fixed slit width of 1 mm.

the delay and attenuation of the magnetic field using low-frequency time-domain simulations in CST Studio Suite [19], calculating the time evolution of the pulsed magnetic field distribution. Figure 3(a) illustrates a 3D model used for the simulation. This model includes Ti strips separated by slits, representing a patterned coating on the inner surface of a chamber with a racetrack-shaped aperture. This design was selected to ensure seamless integration with the ongoing kicker development for SPring-8-II, which utilizes the double-layered lamination core [12]. While an 8 μs wide half-sine excitation is planned in the latest SPring-8-II design, a 4 μs wide half-sine pulse was adopted in this simulation to ensure broader applicability of this work. Figure 3(b) presents the simulation results for Ti strips with a 5 mm width and 10 μm thickness, separated by 1 mm slits. For comparison, results for no coating and a 4 μm thick uniform coating are also shown. The uniform coating caused a significant delay (approximately 1 μs) and an unacceptable 20% reduction in peak amplitude. In contrast, the strip-patterned coating substantially suppressed the field attenuation, even with a 10 μm thickness, by reducing both the eddy current loop size and conductivity.

A detailed comparison with the no-coating case reveals that while the patterned coating results in negligible attenuation of the peak magnetic field strength [Fig. 3(b)], it introduces a non-negligible delay of 1.5 ns in the peak timing. Consequently, the relative deviation in magnetic field strength is more pronounced at the rising and falling edges of the pulse. To quantify the deviation, the maximum deviation at the edges was normalized by the amplitude of the applied half-sine pulse. This normalized deviation is shown in Fig. 4 as a function of the coating thickness for strip widths of 3, 5, and 7 mm, with a fixed slit width of 1 mm. As expected, the results indicate that the deviation caused by eddy currents increases with the strip width. Based on the results in Fig. 4, we determined the patterned Ti coating parameters to meet our requirement for beam injection: a magnetic field deviation of 0.1% or less between the two Ti coated ceramic chambers for the twin kickers. The following parameters were selected: a nominal thickness of 8 μm, a coated strip width of 5 mm, and an uncoated slit width of 1 mm. Although narrower strips are advantageous for suppressing eddy currents, the 3 mm width was rejected in favor of the 5 mm width to reduce beam coupling impedance. The nominal thickness of 8 μm was chosen to accommodate a manufacturing tolerance of ± 2 μm, ensuring the minimum thickness requirement of 6 μm is met. The design target for eddy current suppression at the 8 μm nominal thickness is a field deviation of 0.1% relative to the peak value, as illustrated in Fig. 4.

To realize the optimized coating, a conceptual design was developed for a ceramic vacuum chamber, equipped with metallic vacuum flanges at both ends, as shown in Fig. 5. The chamber comprises a 400 mm long ceramic section with a racetrack-shaped aperture, with its inner surface coated with an 8 μm thick, strip-patterned Ti layer. This pattern consists of 5 mm wide strips separated by 1 mm slits to ensure electrical isolation between them. To prevent the formation of eddy current loops, the entire

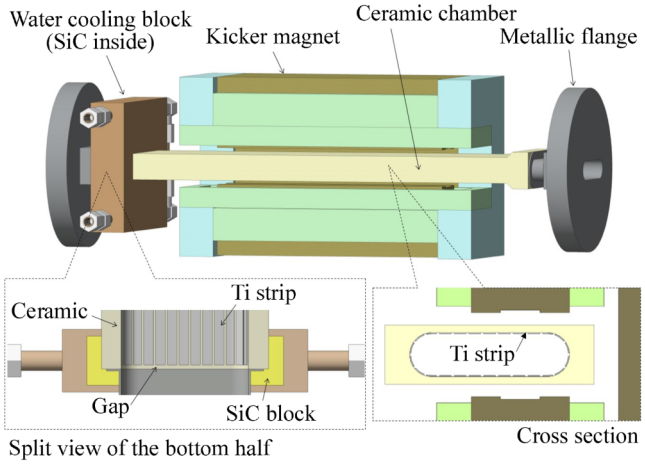

FIG. 5. Conceptual design of the ceramic vacuum chamber and kicker magnet assembly. SiC blocks cover the isolation gap between the Ti strips and the metallic flange at one end of the chamber to absorb rf leakage from wakefields. When installed in a storage ring, this assembly is enclosed by an EMI shield housing for the kicker.

coating pattern was set back from the metallic part by a 1 mm gap at one end. While this isolating gap mitigates eddy currents, it also creates a path for rf leakage from wakefields. To avoid heating of the pulsed kicker due to rf leakage in the electromagnetic interference (EMI) shield housing, rf-absorbing silicon carbide (SiC) blocks are installed around the chamber exterior, covering the gap. The specific heat load was calculated using wakefield simulations in CST assuming the SPring-8-II beam parameters summarized in Table I. The estimated thermal loss is 25 W in the SiC blocks, 11 W on the Ti strips, and 0.1 W inside the ceramic part. A recent study reports that measurement of beam-induced heating is consistent with wakefield simulations [20]. These heat loads are managed via water-cooling for the SiC blocks and forced-air cooling for the ceramic chamber. Under the assumption of a uniform heat distribution of 5.5 W (11 W/2) on both the top and bottom inner surfaces of the ceramic chamber (area: 65×400 mm), a temperature rise was estimated to be 11 K, assuming a heat transfer coefficient of 20 $\mathrm{W}/(\mathrm{m}^2\,\mathrm{K})$. A simplified forced-air cooling simulation in CST indicates that an airflow velocity of 2 m/s within the 5 mm gap defined by the clearance between the magnet pole and the ceramic chamber in the SPring-8-II design, achieves a heat transfer coefficient of approximately 20 $\mathrm{W}/(\mathrm{m}^2\,\mathrm{K})$. The simulation considered thermal conduction in solids and convection in the surrounding air, while surface thermal radiation was neglected. The steady-state temperature rise of the ceramic chamber in the simulation was suppressed to ≤ 10 K. Using wakefield simulations in CST, the effective impedance contribution per chamber to transverse mode coupling instability was evaluated to be 50 kΩ, which is negligible compared to the total effective impedance of approximately 10 MΩ estimated on the entire storage ring.

TABLE I. SPring-8-II beam parameters assumed for heat load and impedance calculations [3].

Bunch current	0.5 mA
Bunch mode	406 bunches/2436 buckets
Bunch repetition time	11.8 ns
Bunch length	14 ps (rms)
Revolution frequency	208.85 kHz
Betatron tune ν_x, ν_y	108.1, 42.58
Betatron function β_x, β_y	0.5, 25 m

III. EXPERIMENTS ON EDDY CURRENT EFFECTS WITH A PROTOTYPE

A. Prototype

We developed a prototype ceramic vacuum chamber to evaluate the penetration of ac magnetic fields, while minimizing eddy currents (Fig. 6). This prototype was designed for testing purposes and was not intended for installation in the storage ring. The chamber comprises a monolithic, high-purity (> 99.5%) alumina (Al_2O_3) body with a racetrack-shaped aperture. Ti vacuum flanges were attached to both ends via Ti sleeves. The sleeves were vacuum-brazed to the ceramic chamber, followed by TIG welding of the flanges to the sleeves. A monolithic ceramic construction was selected over a brazed half-split design to prevent the formation of longitudinal eddy current loops along the brazing seam. An alternative method, such as glass bonding of half-split ceramic pieces, was rejected

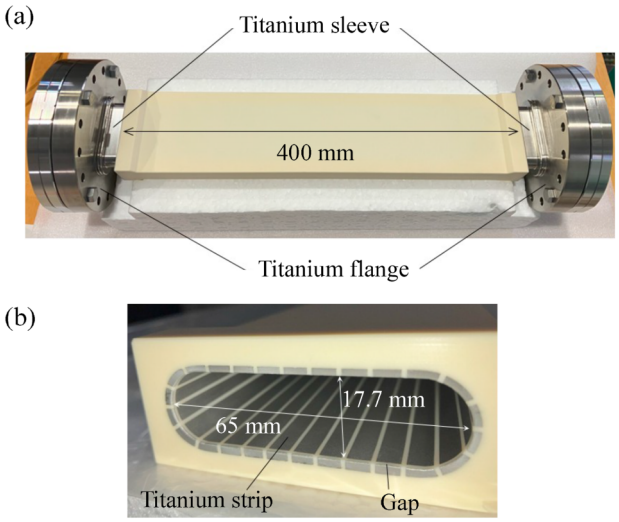

FIG. 6. (a) Prototype ceramic vacuum chamber with Ti flanges connected to both ends via Ti sleeves. (b) Ti strip-patterned coating on the inner surface of the prototype chamber (5 mm strip width, 1 mm slit width). The strips are electrically isolated from the sleeves by a 1 mm gap.

due to the risk of thermal damage to the bond during the subsequent sleeve-brazing process. The inner surface of the ceramic chamber was coated with Ti via magnetron sputtering. The coating was patterned into alternating 5 mm wide Ti strips and 1 mm wide uncoated slits to ensure electrical isolation between the strips. Prior to the prototype fabrication, coating thickness uniformity was investigated by depositing a coating with a target thickness of 8 μm onto racetrack-shaped test ducts with prototype-based geometry. Specific areas were masked before deposition. After sectioning the ducts to access the coated surfaces, the masks were removed and the resulting step heights were measured using a stylus profiler. The thickness was confirmed to be 8 ± 1 μm.

To prevent the formation of eddy current loops involving the coating and the sleeves, and to facilitate isolation measurements, the entire coated pattern was set back by a 1 mm gap from the sleeves at both ends. Since rf leakage from wakefields through this isolation gap is not a concern for the intended magnetic performance measurements, the rf-absorbing SiC blocks were omitted from the prototype design. For comparison of eddy current effects, a bare ceramic chamber without the strip-patterned coating or flanges was also prepared.

B. Experiments

Figure 7 shows an experimental setup designed to quantitatively investigate the effect of Ti strip-patterned coating of the prototype chamber on the pulsed magnetic field of a kicker magnet. The chamber was positioned in the pole gap of a laminated-core magnet, and a long search coil (5×460 mm), fabricated on a printed circuit board (PCB) measuring 20×490 mm with a trace width of 0.1 mm, was inserted into the chamber aperture. The PCB was mounted on a Bakelite plate equipped with

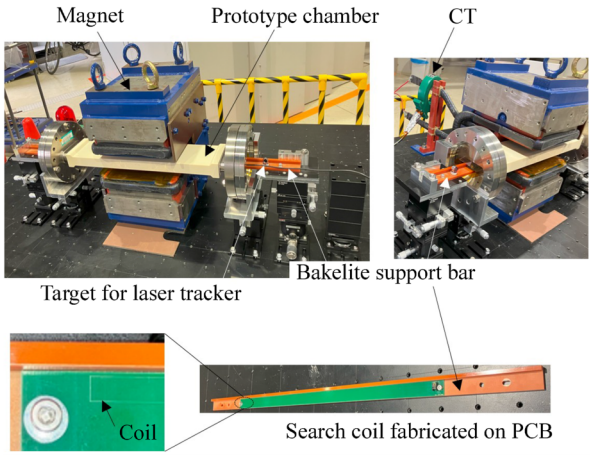

FIG. 7. Experimental setup for measuring the pulsed magnetic field strength. The search coil is inserted into the prototype chamber positioned within the kicker magnet gap. The coil's position relative to the magnet was aligned using a laser tracker.

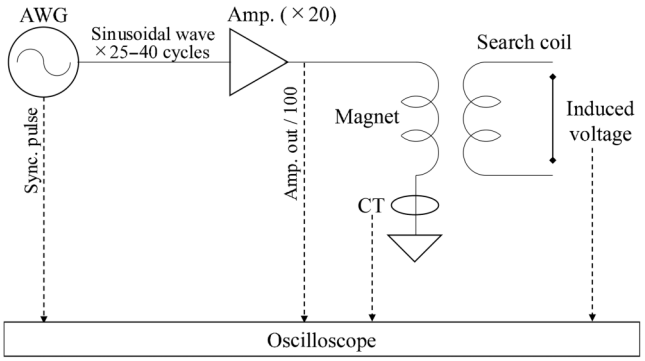

FIG. 8. Schematic circuit diagram of the measurement setup utilizing low-current sinusoidal excitation.

laser-tracker targets at both ends. The coil's position relative to the magnet was precisely aligned using a laser tracker to ensure consistency throughout the measurements. A current transformer (CT) was installed on the wire of the kicker magnet coil.

Measuring small relative differences of 0.1% or less in the pulsed magnetic field strength presents a technical challenge. We employed low-current sinusoidal excitation instead of driving the magnet at its nominal current. This approach mitigates the impact of local measurement environment during the operation of high-voltage pulsed power supplies. Figure 8 illustrates a schematic circuit diagram of the measurement setup using a small sinusoidal excitation current. A sinusoidal voltage signal generated by an arbitrary waveform generator (AWG, Agilent 33220A) was amplified by a bipolar amplifier (NF HSA4014) before being applied to the magnet. The excitation current was monitored using the CT (Pearson 110A). An induced voltage across the search coil, proportional to the time derivative of the magnetic flux, was monitored simultaneously. An oscilloscope (Tektronix MSO44) recorded the output signals from both the CT and the search coil. The oscilloscope was triggered via either the amplifier's monitor output (1/100 attenuation) or a synchronous pulse from the AWG. Data acquisition was performed with a sampling interval of 0.32 ns and a bandwidth limit of 20 MHz. Each measurement comprised 25–40 periods of a 125 kHz sinusoidal wave, a frequency corresponding to the dominant component of the intended 4 μs half-sine excitation.

Figure 9 displays typical oscilloscope traces, showing the CT (orange), induced voltage across the search coil (cyan), the 1/100-attenuated amplifier voltage (yellow), and the AWG synchronous pulse (green), with offsets for visibility. The excitation current monitored by the CT exhibits a transient response at the onset of excitation. A measured time constant of this response is 15 μs, consistent with the value derived from equivalent RL series circuit parameters (3 μH/0.2 Ω) of the magnet which was measured separately using an LCR meter

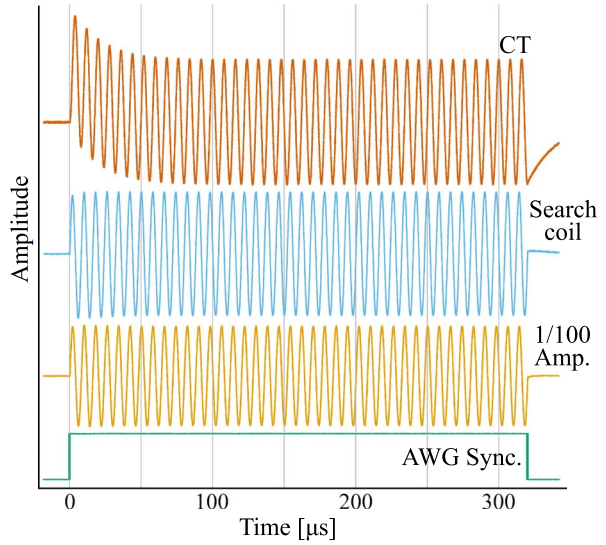

FIG. 9. Measured oscilloscope traces: excitation current from the CT (orange), induced voltage across the search coil (cyan), the 1/100-attenuated amplifier voltage (yellow), and the AWG synchronous pulse (green), with offsets for visibility.

(NF ZM2375). A steady-state period was defined as the interval starting 140 μs after the excitation onset. At this point, the transient response decays to a negligible level $\exp(-140\ \mu s/15\ \mu s) < 10^{-4}$, which is 1 order of magnitude smaller than the target precision of 0.1%. Consequently, subsequent analyses were restricted to the data acquired during this steady-state period.

Experiments were performed under three configurations: (i) with the prototype chamber, (ii) with the bare chamber, and (iii) without any chamber. The magnetic field was evaluated by analyzing the output voltage of the search coil. The use of continuous sinusoidal excitation allows fast Fourier transform (FFT) analysis to precisely extract the magnitude and phase of the fundamental frequency for each measurement. This approach facilitates the comparison of small relative differences by mitigating interference from random offset voltage drift and trigger jitter. The observed dominance of the fundamental frequency ($f = 125$ kHz) indicates that waveform distortion arising from system nonlinearity (e.g., amplifier saturation) was negligible, thereby validating this analysis method. For each measurement, the magnitude of the fundamental component of the search coil output, M_{sc}, was normalized by the corresponding CT magnitude, M_{ct}, yielding the normalized magnitude $M_{\mathrm{norm}} = M_{\mathrm{sc}}/M_{\mathrm{ct}}$. This normalization effectively compensates for excitation current fluctuations originating from the AWG or the amplifier.

Comparisons were made between the averages of the normalized magnitudes, $M_{\mathrm{norm_avg}}$, obtained from measurements acquired on the same day. For a comparison between conditions (i) and (ii) with 40 measurements each, the relative difference in magnetic field amplitude, Δ_M, was defined as

$$\Delta_M = \frac{M_{\mathrm{norm_avg(i)}} - M_{\mathrm{norm_avg(ii)}}}{(M_{\mathrm{norm_avg(i)}} + M_{\mathrm{norm_avg(ii)}})/2}. \tag{3}$$

The statistical uncertainty of $M_{\mathrm{norm_avg}}$ was conservatively estimated as the standard deviation of the repeated M_{norm} measurements ($\leq 0.05\%$ for all measurements summarized in Table II); this uncertainty was propagated to the relative difference. The phase difference ϕ_{dif} between the search coil output ϕ_{sc} and the CT output ϕ_{ct} was also calculated for each measurement as $\phi_{\mathrm{dif}} = \phi_{\mathrm{sc}} - \phi_{\mathrm{ct}}$. The averaged phase difference $\phi_{\mathrm{dif_avg}}$ was evaluated, with the uncertainty represented by the standard deviation of the repeated measurements. The time delay Δ_ϕ (in seconds) was derived using $\Delta_\phi = -(\phi_{\mathrm{dif_avg(i)}} - \phi_{\mathrm{dif_avg(ii)}})/2\pi f$.

Figures 10(a) and 10(b) visualize Δ_M and Δ_ϕ, respectively, with error bars corresponding to the statistical uncertainties, for various comparison pairs listed in Table II. Experimental details, including the number of repeated measurements, the number of AWG sinusoidal excitation cycles, and oscilloscope trigger signal, are also summarized in Table II. To quantify systematic errors associated with magnitude evaluation, we investigated a gain factor derived from FFT magnitude data, defined as the ratio of the amplifier output magnitude to that of the CT output. Variations in this gain factor could be primarily attributed to temperature fluctuations in both the amplifier

TABLE II. Summary of experimental details for various comparison pairs.

No.	Comparison pair	Number of measurements	AWG cycles	Oscilloscope trigger
1	Prototype-Bare	20, 20	40	AWG Sync.
2	Prototype-Bare	20, 20	25	Amp./100
3	Prototype-No chamber	40, 40	25	Amp./100
4	Prototype-No chamber	40, 40	25	Amp./100
5	Prototype-No chamber	40, 40	25	Amp./100
6	Prototype-No chamber	40, 40	25	Amp./100
7	Bare-No chamber	40, 40	25	Amp./100
8	Bare-No chamber	40, 40	25	Amp./100

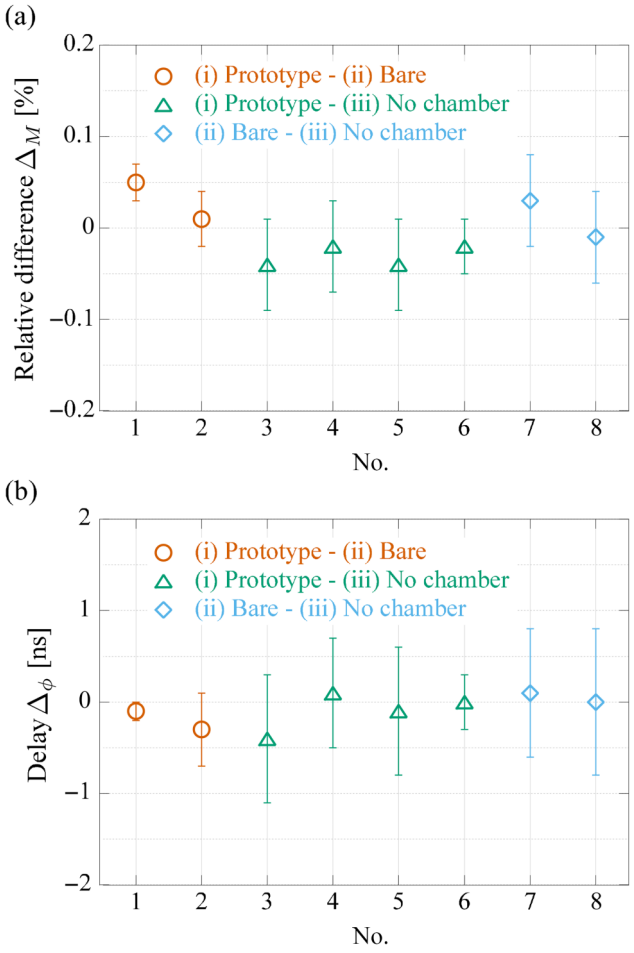

FIG. 10. Comparison of the three experimental conditions: (i) prototype chamber, (ii) bare chamber, and (iii) no chamber. Plots show (a) the relative difference in the magnitude of the normalized search coil signal and (b) the time delay. Error bars represent the propagated standard deviations of repeated measurements under the same conditions.

and the oscilloscope. The gain factor exhibited variations of up to 0.05% across the eight datasets listed in Table II.

The observed relative differences in normalized search coil signal magnitude, specifically for pairs (i) and (ii) and (i)–(iii) in Fig. 10(a) evaluated to assess the Ti strip coating effect, fall within the 0.05% systematic uncertainty range. We therefore confirmed that the magnetic field amplitude deviation caused by the Ti strip coating remains within ±0.1%, consistent with the design target. Regarding the time delay for pairs (i) and (ii) and (i)–(iii) in Fig. 10(b), the results exhibit a slight discrepancy compared to the 1.5 ns delay predicted by the CST simulations for the half-sine excitation of 4 μs, even when accounting for statistical fluctuations of up to 0.8 ns. While the cause of this discrepancy remains under investigation, the observed delay was shorter than predicted. Consequently, the signal difference resulting from this delay is within 0.1% of the peak value.

For the SPring-8-II application, the kicker magnet is designed to operate with a half-sine pulsed magnetic field. In such a system, deviation from the ideal waveform, such as an undershoot at the falling edge, introduces high-frequency components. These components compromise the suppression of eddy currents. Consequently, the design of the entire system, including the power supply, is required to minimize deviations from the ideal waveform. To demonstrate the feasibility of this approach, we conducted a preliminary study using a 4 μs half-sine waveform generated by a test circuit, designed for pulsed drive via capacitor discharge, using a MOSFET switch with a discrete push-pull gate driver. This circuit replaced the AWG and amplifier used for the previous sinusoidal excitation measurements, enabling the generation of a more realistic pulsed waveform. Forty measurement pairs were acquired with alternating magnetic field polarity for both the prototype and bare chambers. The search coil signals from each pair were subtracted to eliminate any common-mode noise that could compromise the measurement accuracy without obscuring any physical effects. The resulting data were averaged over the 40 pairs at each sampling point. The averaged voltage signals were time-integrated and divided by the coil width to derive effective field integral BL (T m) along the coil length.

Figure 11 displays the results. The relative difference between the prototype and bare chambers was normalized by the combined average peak value of the two chambers. The difference was typically less than 0.1% throughout the pulse duration with maximum deviation of 0.11%, consistent with the design target. The standard deviations, calculated from the multiple measurements taken before averaging, remained within 0.1% of their respective averaged peak values for both the CT and magnetic field data at each sampling point. The results of this preliminary experiment are promising. We conclude that the Ti strip-patterned coating developed in this study is capable of limiting eddy-current-induced magnetic field deviations to

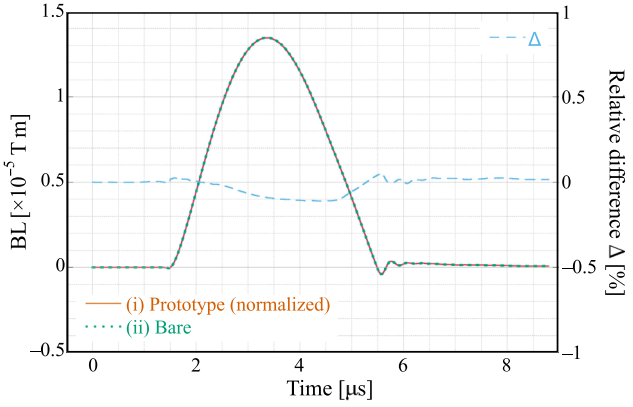

FIG. 11. Effective field integral BL along the coil length for the prototype and bare chambers, derived from time-integrated search coil signals averaged over the 40 pairs.

approximately 0.1% of the peak value throughout pulse duration as short as 4 μs. The prototype chamber successfully demonstrated this performance with a maximum deviation of 0.11%.

The magnetic field performance of the prototype chamber was evaluated using two complementary experimental setups. First, measurements with repetitive sinusoidal excitations followed by FFT analysis enabled a precise quantitative comparison of the dominant fundamental frequency component corresponding to the kicker pulse duration, by averaging out shot-to-shot fluctuations. Second, measurements using the custom-built half-sine pulse circuit enabled a feasibility study of more realistic pulsed excitations with deviations from the ideal waveform, such as an undershoot at the falling edge. Consequently, we conclude that the prototype chamber meets the design target, limiting the magnetic field deviation due to eddy currents to within approximately 0.1% of the peak value for pulsed excitations as short as 4 μs.

IV. SUMMARY

Mitigating magnetic field distortion from eddy currents while reducing beam coupling impedance and heat load is a primary challenge for both traditional pulsed dipole and nonlinear kickers. We designed and prototyped a ceramic vacuum chamber, achieving magnetic transparency for external kicker pulses as short as 4 μs while suppressing impedance. With the appropriate optimization of the strip configuration tailored to specific facility requirements, the patterned coating provides a solution to reconcile the conflicting requirements of magnetic transparency, low impedance, and thermal management in next-generation light sources.

The prototype was designed to meet the requirement for SPring-8-II: closing the injection orbit bump by suppressing the magnetic field deviations between multiple kickers to within 0.1% of the peak amplitude throughout the bump duration. To achieve this, we applied a strip-patterned Ti coating to the inner surface of the ceramic chamber, with the strip thickness and width optimized via simulations using CST studio suite. The optimized design features an 8 μm thick layer with 5 mm wide strips separated by 1 mm slits. This configuration satisfies the minimum thickness requirement (at least 6 μm) for heat suppression while simultaneously minimizing magnetic field distortions caused by eddy currents.

To validate the magnetic performance, a prototype chamber was fabricated and measured using a search coil under 125 kHz sinusoidal excitation, which represents the dominant frequency component of the 4 μs half-sine waveform. FFT analysis confirmed that the magnetic field deviation caused by eddy currents in the strip-patterned Ti coating was suppressed to within ±0.1% of the peak amplitude. Furthermore, the potential impact of transient characteristics under realistic pulsed excitation was evaluated using a waveform simulating a 4 μs half-sine pulse to assess the feasibility. The resulting deviation was found to be approximately 0.1%, confirming its practical applicability.

The ceramic vacuum chamber developed in this study will be implemented in the twin-kicker magnet system to enable transparent off-axis beam injection in SPring-8-II. The overall transparency of beam injection, as well as the heat load at the designed beam current of SPring-8-II, will be evaluated during the upcoming commissioning phase and reported in future publications.

ACKNOWLEDGMENTS

The authors would like to express their gratitude to Dr. Tetsuya Ishikawa, Director of the RIKEN SPring-8 Center (RSC), and Dr. Kazuto Yamauchi, Professor of Osaka University-RIKEN Center for Science and Technology, for their instrumental roles in connecting us with JTEC Corporation [21], which devised the process for the patterned coating from the R&D stage. This contribution was essential to the success of this work. We would also like to thank Dr. Takahiro Watanabe, Director of the Accelerator Division of JASRI, for his insightful comments and continuous encouragement, as well as the staff at RSC and JASRI for their valuable suggestions and support. This work was supported by RSC.

DATA AVAILABILITY

The data that support the findings of this article are not publicly available. The data are available from the authors upon reasonable request.

[1] P. Raimondi, N. Carmignani, L. R. Carver, J. Chavanne, L. Farvacque, G. Le Bec, D. Martin, S. M. Liuzzo, T. Perron, and S. White, Commissioning of the hybrid multibend achromat lattice at the European Synchrotron Radiation Facility, Phys. Rev. Accel. Beams **24**, 110701 (2021).

[2] T. E. Fornek, Advanced photon source upgrade project final design report, Technical Report, Argonne National Laboratory (ANL), Argonne, IL (United States), 2019.

[3] H. Tanaka *et al.*, Green upgrading of SPring-8 to produce stable, ultrabrilliant hard X-ray beams, J. Synchrotron Radiat. **31**, 1420 (2024).

[4] C. G. Schroer, I. Agapov, W. Brefeld, R. Brinkmann, Y.-C. Chae, H.-C. Chao, M. Eriksson, J. Keil, X. N. Gavaldà, R. Röhlsberger, O. H. Seeck, M. Sprung, M. Tischer, R. Wanzenberg, and E. Weckert, PETRA IV: The ultralow-emittance source project at DESY, J. Synchrotron Radiat. **25**, 1277 (2018).

[5] T. Atkinson, M. Dirsat, O. Dressler, P. Kuske, and H. Rast, Development of a non-linear kicker system to facilitate a new injection scheme for the BESSY II storage ring, in *Proceedings of the 2nd International Particle Accelerator*

Conference, (JACoW Publishing, Geneva, Switzerland, 2011), pp. 3394–3396.

[6] P. Alexandre, R. B. E. Fekih, A. Letrésor, S. Thoraud, J. S. Castro, F. Bouvet, J. Breunlin, and P. F. Tavares, Transparent top-up injection into a fourth-generation storage ring, Nucl. Instrum. Methods Phys. Res., Sect. A **986**, 164739 (2021).

[7] L. Liu, M. B. Alves, F. C. Arroyo, G. O. Brunheira, G. R. Cruz, A. F. Giachero, A. C. S. Oliveira, F. S. de Oliveira, G. S. Ramirez, X. R. Resende, E. N. Rolim, F. H. de Sá, D. O. Tavares, and H. Westfahl Jr., Status of SIRIUS operation with users, in *Proceedings of the 14th International Particle Accelerator Conference* (JACoW Publishing, Geneva, Switzerland, 2023), pp. 2586–2589.

[8] R. Ollier, P. Alexandre, R. B. E. Fekih, A. Gamelin, N. Hubert, M. Labat, L. S. Nadolski, and M.-A. Tordeux, Toward transparent injection with a multipole injection kicker in a storage ring, Phys. Rev. Accel. Beams **26**, 020101 (2023).

[9] S. Takano, K. Fukami, C. Kondo, M. Masaki, M. Oishi, M. Shoji, K. Tamura, T. Taniuchi, T. Watanabe, K. Yanagida, H. Akikawa, K. Sato, T. Hara, T. Inagaki, H. Tanaka, K. Hamato, J. Kataoka, K. Kusano, K. Ogata, and Y. Saito, Renovation of off-axis beam injection scheme for next-generation photon sources, in *Proceedings of the 10th International Particle Accelerator Conference* (JACoW Publishing, Geneva, Switzerland, 2019), pp. 2318–2321.

[10] T. Hara *et al.*, Low-emittance beam injection for a synchrotron radiation source using an X-ray free-electron laser linear accelerator, Phys. Rev. Accel. Beams **24**, 110702 (2021).

[11] H. Tanaka *et al.*, Stable top-up operation at SPring-8, J. Synchrotron Rad. **13**, 378 (2006).

[12] K. Fukami, T. Inagaki, T. Iwashita, H. Nakanishi, N. Nishimori, S. Takano, Y. Takemura, T. Taniuchi, T. Watanabe, H. Yamaguchi, and H. Tanaka, Iron lamination and interlaminar insulation for high-frequency pulsed magnets, Rev. Sci. Instrum. **93**, 023301 (2022).

[13] T. Inagaki, H. Tanaka, H. Akikawa, K. Sato, K. Fukami, C. Kondo, and S. Takano, Development of a solid-state pulse generator driving kicker magnets for a novel injection system of a low emittance storage ring, in *Proceedings of the 9th International Particle Accelerator Conference* (JACoW Publishing, Geneva, Switzerland, 2018), pp. 1804–1807).

[14] L. Walling, D. Neuffer, H. A. Thiessen, and G. Spalek, Transmission-line impedance measurements of beam pipes for an advanced hadron facility, in *Proceedings of the IEEE Particle Accelerator Conference* (1987), pp. 1164–1166, https://proceedings.jacow.org/p87/PDF/PAC1987_1164.PDF.

[15] J. E. Milburn, M. Yoon, and Y. S. Kim, Patterned metallic coating of a ceramic chamber in storage ring bump magnets, IEEE. Trans. Nucl. Sci. **47**, 2715 (2000).

[16] C. Mitsuda, H. Takaki, R. Takai, T. Nogami, T. Uchiyama, Y. Kobayashi, T. Obina, Y. Lu, and A. Yokoyama, Suppression of eddy-current effects in beam injection using a pulsed sextupole magnet with a new ceramic chamber, Phys. Rev. Accel. Beams **25**, 112401 (2022).

[17] Z. Chen, P. Tian, Y. Yang, Y. Ma, X. Peng, G. Wu, S. Yue, J. Chen, N. Wang, and P. He, Development of ceramic vacuum chamber for collider ring kicker of circular electron positron collider (CEPC), Vacuum **214**, 112247 (2023).

[18] R. Nagaoka and K. L. F. Bane, Collective effects in a diffraction-limited storage ring, J. Synchrotron Radiat. **21**, 937 (2014).

[19] Dassault Systèmes, CST studio suite, https://www.3ds.com/products/simulia/cst-studio-suite.

[20] A. Khan, G. Bassi, B. Kosciuk, R. Todd, V. Smaluk, B. Bacha, P. Palecek, and C. Hetzel, Simulation and measurement of beam-induced heating of ceramic vacuum chambers, Phys. Rev. Accel. Beams **27**, 084501 (2024).

[21] JTEC Corporation, https://www.j-tec.co.jp/english/.